

DIGITAL MICROFLUIDIC DESIGN FOR INJECTION CONTINUOUS LIQUID INTERFACE PRODUCTION OF 3D OBJECTS

Gabriel Lipkowitz¹, Tim Samuelsen¹, Kaiwen Hsiao², Maria T. Dulay², Ian Coates³,
William Pan¹, Eric S.G. Shaqfeh^{1,3}, Joseph M. DeSimone^{2,3}

¹ Department of Mechanical Engineering, Stanford University, Stanford, CA 94305

² Department of Radiology, Stanford University, Stanford, CA 94305

³ Department of Chemical Engineering, Stanford University, Stanford, CA 94305

Abstract

In additive manufacturing, it is imperative to increase print speeds, use higher viscosity resins, and print with multiple different resins simultaneously. To this end, we introduce a new UV-based photopolymerization 3D printing process exploiting a continuous liquid interface—the deadzone—mechanically fed with resin at elevated pressures through microfluidic channels dynamically created and integral to the growing part. Through such mass transport control, injection continuous liquid interface production, or iCLIP, accelerates printing speeds 5 to 10-fold over current methods such as continuous liquid interface production (CLIP), can utilize resins an order of magnitude more viscous than can CLIP, and can readily pattern a single heterogeneous object with different resins in all Cartesian coordinates. We characterize the process parameters governing iCLIP and demonstrate use-cases for rapidly printing carbon nanotube-filled composites, multi-material features with length scales spanning several orders of magnitude, and lattices with tuneable moduli and energy absorption.

Keywords: injection continuous liquid interface production (iCLIP), continuous liquid interface production (CLIP), generative design, parametric design, algorithmic design, additive manufacturing, microfluidics

Introduction

UV curable liquid resin-based additive manufacturing (AM) can broadly be divided into three generations of vat photopolymerization (1) and material jetting. In first generation vat photopolymerization (VP), also known as stereolithography (SLA), a bath containing a single liquid resin is photocured spatio-selectively by a scanning laser point source. Second generation VP, referred to as digital light projection (DLP), uses a rapid sequence of projected UV images that span the entire X-Y plane of a bath containing a liquid resin in a single exposure. Often referred to as third generation VP, continuous liquid interface production (CLIP, **Figure 1a**) relies on resin renewal at the build surface through a continuous liquid interface—the dead zone—created by oxygen, a polymerization inhibitor, fed through the oxygen-permeable window beneath the vat (2-4). CLIP, achievable with multiple patterns of platform movement and UV exposure (5) along with different window configurations (6, 7), enables printing at speeds up to 3000 mm/hr, 25 to 100 times higher than traditional AM methods. While to date CLIP has been limited to relatively low viscosity resins (commercially available resins from Carbon, Inc. have viscosities up to roughly 2500 cP) (8), CLIP produces isotropic parts, unlike conventional 3D printing methods like fused filament fabrication (FFF) and powder bed fusion (PBF), and has proven suitable for manufacturing at high volumes and at high resolution for *e.g.* biomedical devices (9,10).

However, CLIP is still significantly slower than injection molding. This is due to severe mass transport limitations on resin flow through the thin dead zone (**Figure 1b**), inducing Stefan adhesion forces that require delay time to equilibrate the negative dead-zone pressure. These forces also limit print sizes and necessitate cumbersome supporting scaffolds as in traditional VP techniques (11, 12). From lubrication theory, this Stefan adhesion force scales dramatically with part radius:

$$F_{\text{Stefan}} = \frac{-3\pi R^4 \mu U}{2h^3} \quad (1)$$

where R is part radius, μ resin viscosity, U print speed, and h dead zone thickness. These mass transport limitations, though intensely examined in the literature (13-15), restrict CLIP and VP from efficiently processing highly filled composite resins, and from effectively printing with multi-materials.

In the second UV resin-based AM approach, material jetting (MJ), an inkjet print head deposits photocurable resin droplets onto a build surface, readily printing with high spatial control, multi-materials, and highly viscous filled composites (16-18). Disadvantages of MJ, however, include highly anisotropic part properties and very slow printing, making it difficult to scale and arguably mainly for prototyping.

Here we describe our new AM method that synthesizes these two established AM approaches by injecting resin through CAD software-designed microfluidic conduits in the part, or “viaducts”, into a continuous liquid interface to supply part production (**Figure 1b**). Like CLIP, this method uses a highly oxygen permeable window to create a deadzone that, in this instance, provides a destination for resin flow from our high pressure fluidic injection system (**Figure 1c**). We call this 3D printing approach injection continuous liquid interface production, or iCLIP for short.

Results and Discussion

Injection into a deadzone alleviates suction forces to accelerate printing of 3D geometries

An apparatus for testing the iCLIP printing process is described in **Figure 2a**. In this system, without high-pressure injection, we recapitulate a traditional CLIP process, and suction forces scale with part cross sectional area, as expected from the aforementioned lubrication theory (**Figure 2b**). Without limiting volumetric print speeds, significant defects and premature delamination from the platform can result.

Herein we show that a single viaduct can offset these forces. From lubrication theory, one can determine that a single viaduct, whose area can be varied dynamically by software during printing, introduces a positive pressure increment by administering resin at a volumetric flow rate Q , according to:

$$P_{\text{viaduct}} \sim \frac{\mu L Q}{A h^3} \quad (2)$$

where μ is resin viscosity, L part length, A viaduct area, and h dead zone thickness. Dead zone thicknesses in iCLIP are very small, as in traditional CLIP and as expected from analytical models (19), typically on the order of tens of microns. With injection, lubrication theory predicts the (non-dimensionalized) pressure field in the deadzone to be:

$$\tilde{p}(\tilde{r}) = 6Q\beta^2 \ln\left(\frac{1}{\tilde{r}}\right) + 3(\tilde{r}^2 - 1) \quad (3)$$

where \tilde{p} is pressure, \tilde{r} radial position, Q administered resin flow rate relative to part draw rate, and β viaduct radius relative to part radius. According to **Equation 3**, the positive pressure increment from injection to offset Stefan adhesion forces is directly proportional to the flow rate administered, along with the relative size of the duct facilitating flow, and decays with distance from the duct. Integrated over the newly cured part surface, we obtain a revised (non-dimensionalized) Stefan adhesion force:

$$\tilde{F}_{Stefan}^{iCLIP} = \int_{r=0}^{r=1} \int_{\theta=0}^{\theta=2\pi} \tilde{p}(\tilde{r}) = \frac{\pi(\beta^2 Q - 3)}{2} \quad (4)$$

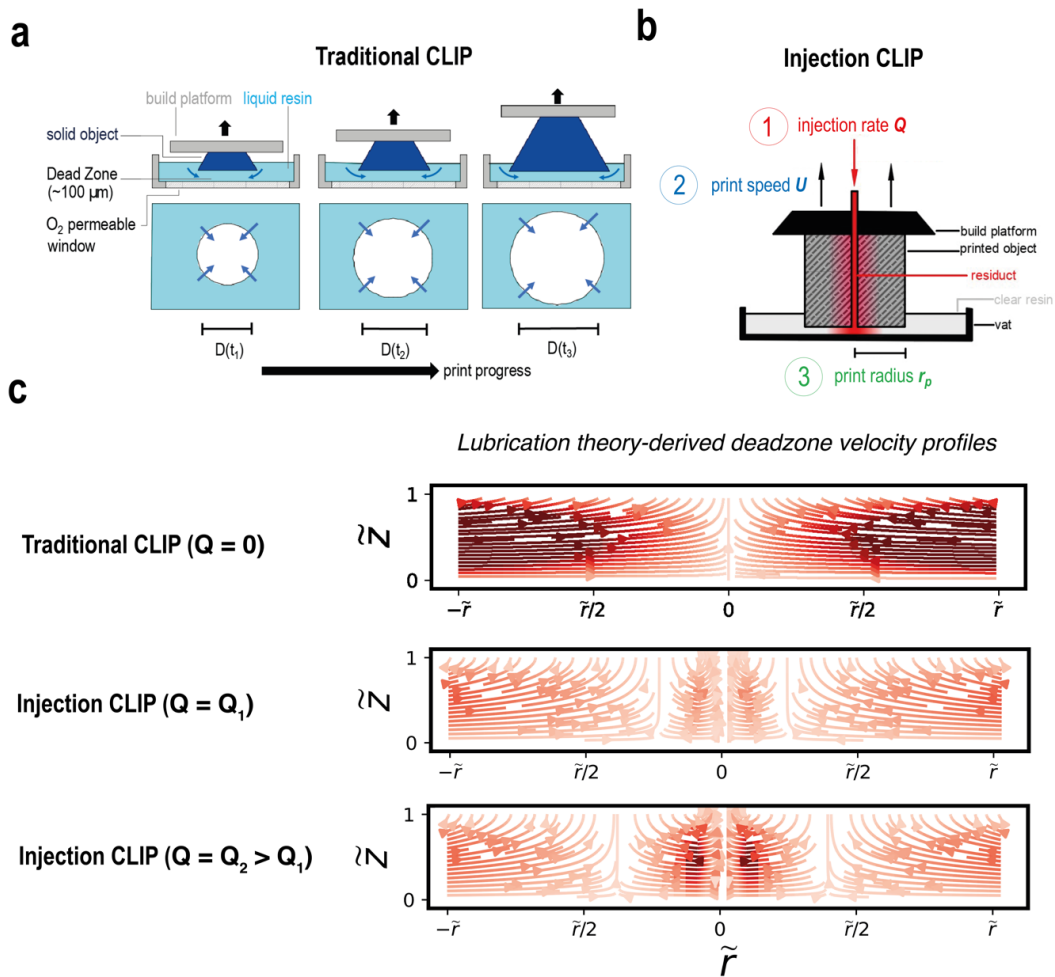


Figure 1: Injection continuous liquid interface production. (a) Traditional CLIP process, which relies on resin renewal at the build surface through a continuous liquid interface—the dead zone—created by oxygen, a polymerization inhibitor, fed through the oxygen-permeable window beneath the vat. (b) Injection CLIP process indicating the flow of injected resin from a pressurized source through microfluidic ducts engineered within the growing part into the dead zone. (c) Analytically-derived dead zone velocity fields from lubrication theory during traditional CLIP (left) and Injection CLIP with continuous injection at two different

volumetric flow rates through a central viaduct (center and right), where z and r are vertical and radial distances in the deadzone, respectively, and v_r is radial velocity.

We find this positive pressure increment indeed allows iCLIP to significantly reduce Stefan adhesion forces—for large area parts by almost two orders of magnitude (**Figure 2c**). While we still observe some scaling of measured Stefan adhesion forces with part cross sectional area, this scaling is much less dramatic than in traditional CLIP.

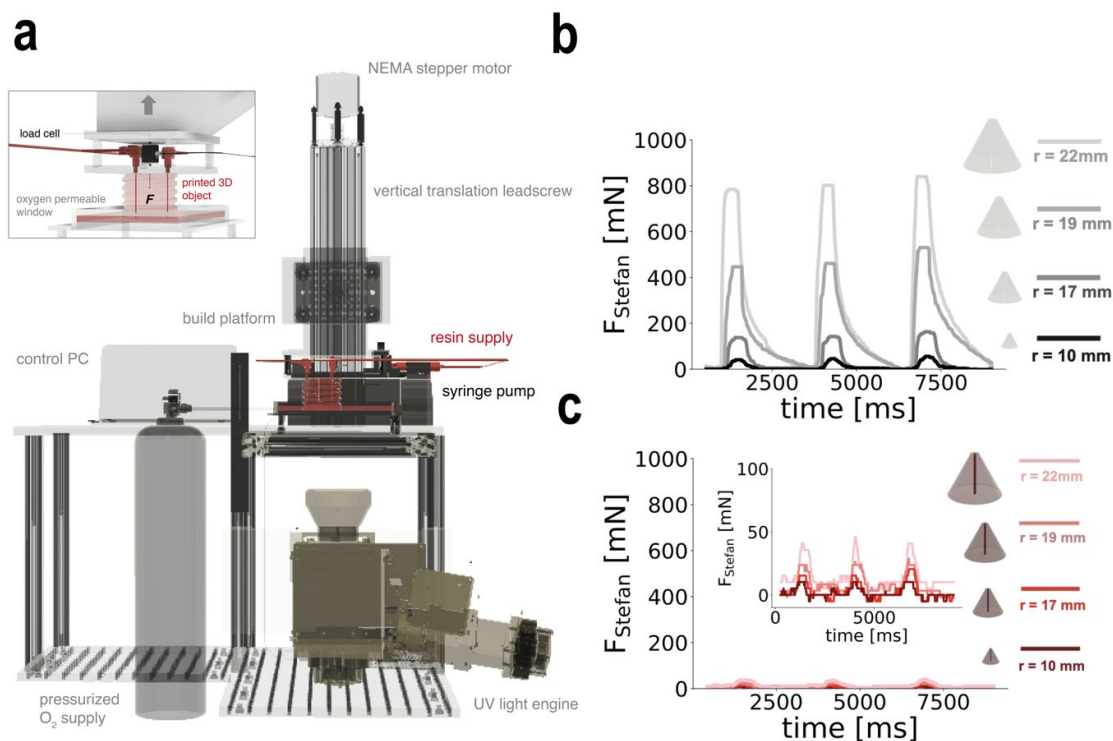


Figure 2: iCLIP alleviates suction forces that plague the traditional CLIP process. (a) Design of a prototype iCLIP printer, with overall hardware configuration and salient features of the iCLIP system highlighted. In upper left, the build region of the iCLIP printer, with the mounting of the load cell and fluidic connectivity ports indicated. The downwards Stefan adhesion force measured by the load cell is indicated by the black arrow, while the platform movement is indicated in grey. **(b-c)** Experimental load cell force data measured for three consecutive layers, each of 3 second duration, while printing a conical geometry with varying cross sectional areas by CLIP and iCLIP, respectively.

These resin injection ducts enable a significant reduction in suction forces that in turn allows iCLIP to achieve significant increases in print speed. For both CLIP and iCLIP, maximum printable speeds for a given cross sectional area can be quantified as the part draw rate at which delamination events occur, at statistically significant levels, for multiple primitive geometries. Injecting resin through a single central viaduct, guided by computational fluid dynamic simulations (**Figure 3a-d**) we observe increases in the maximum achievable print rates determined to be between 5 and 10-fold (**Figure 3e-h**) over CLIP. For a solid conical part with a cross sectional radius growing from 2 mm to 20 mm, for instance, the maximum linear print speed with traditional CLIP before delamination occurs is ~20 mm/hr. With iCLIP, by

contrast, maximum print speeds up to ~ 125 mm/hr are achievable. With a single resin injection channel, delamination does still occur at an elevated print speed for a given part cross sectional area due to the difficulties in administering sufficient resin flow through a single duct, a shortcoming that can be overcome by more complex duct geometries, which is a topic of ongoing investigation.

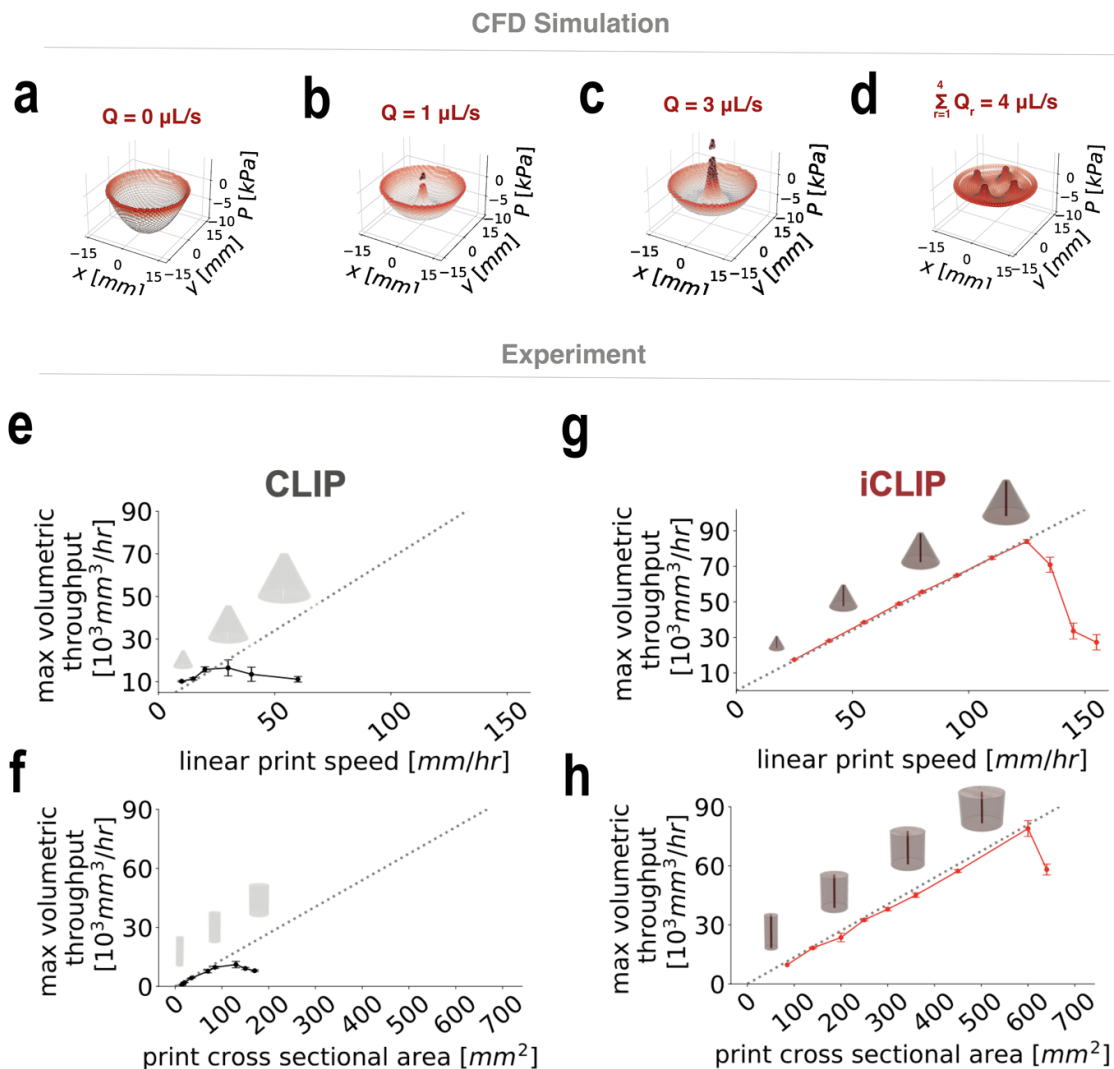


Figure 3: Injection accelerates printing of solid 3D geometries by CLIP. (a-d)

Computational fluid dynamics predictions of the pressure fields experienced while printing a solid circular cross section by traditional CLIP without injection (a), by injection CLIP with flow through a central duct at varying volumetric flow rates (b-c), and by injection CLIP with flow through four distributed ducts at equal flow rates (d). (e-h) Quantified maximum print volumetric throughputs for two test geometries with varying cross sectional areas, cone (e, g) and cylinder (f, h), by CLIP (left) and iCLIP (right). Grey dotted lines indicate delamination-free prints. Error bars denote \pm one standard deviation from three independent print trials.

Importantly, such ducts need not have detrimental impacts on the mechanical properties of the final part with appropriate post-processing. In this study, viaduct channels were

always sealed after printing by utilizing a post-printing UV cure of the resin-filled channels. When such standard protocols are followed, we do not observe any difference in mechanical properties between CLIP and iCLIP printed dogbones, as shown in **Figure 4**.

The requirement to integrate ducts into a part can impact the resolution of iCLIP in comparison with CLIP traditionally, but with careful design strategies, this can be minimized. In areas of the part where ducts must be included, feature resolution does drop to the minimum achievable channel diameter before concerns arise such as capillary collapse, if the channel is freestanding, or channel cure-through, if the channel is embedded. Moreover, viaduct channels can be designed to have larger radii than this achievable minimum, because of the challenges associated with enforcing viscous flow through a narrow channel, according to the Hagan-Poiseuille equation:

$$\Delta P = \frac{8\mu LQ}{\pi R^4} \quad (5)$$

where P is pressure, μ dynamic viscosity, L channel length, Q flow rate, and R channel radius. Flow rates typically range, in this study's experiments, from 7 $\mu\text{L/s}$ to 27 $\mu\text{L/s}$.

While such channels can therefore be detrimental to iCLIP resolution in some circumstances, it is important to note that ducts need not be engineered into all regions of an iCLIP part. Here, the native feature resolution of a traditional CLIP process generalizes to this new printing platform, along with the same tradeoff between print speed and feature resolution as characterized by its inventors (2). Given that the smallest features are indeed those that experience the smallest Stefan adhesion forces, which thus do not likely require active injection to offset, such high resolution features can be preserved in iCLIP parts. Thanks to the software-guided nature of the integration of ducts into iCLIP parts, moreover, ducts can be designed to avoid such high resolution features.

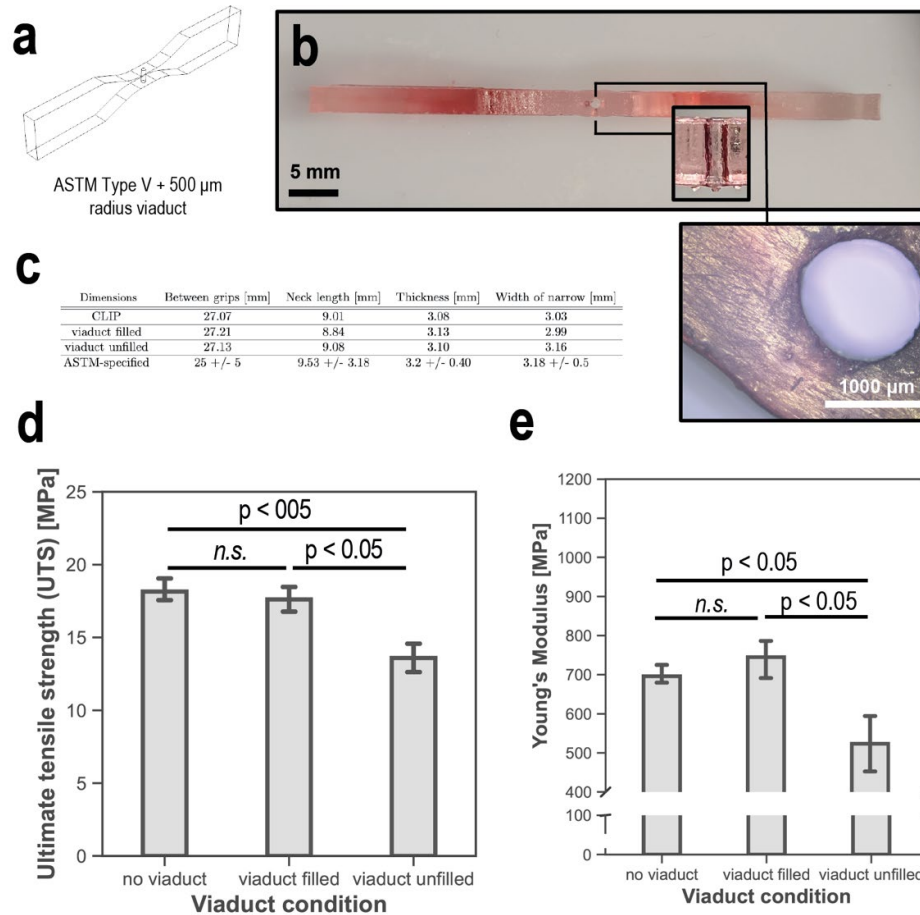


Figure 4: Negligible impact of post-cured viaduct on iCLIP printed part mechanical properties. (a) CAD design of test geometry for evaluating effect of viaduct on dogbone mechanical properties. (b) Picture of iCLIP printed dogbone, with inset showing optical microscopy image of central viaduct. (c) Comparison of iCLIP printed dogbone with ASTM Type V specifications. (d-e) Ultimate tensile strength and Young's modulus, respectively, of iCLIP printed dogbones under different viaduct post-treatment conditions. All measurements represent the average of three independently printed dogbones, with error bars denoting +/- one standard deviation from the mean.

Conclusion

In summary, we describe here iCLIP, a novel 3D printing method using active control of mass transport during continuous liquid interface printing to enhance print speeds. Ongoing work in optimizing the existing iCLIP process focuses on detailed modeling of the flow boundaries in the deadzone, optimizing flow rates to minimize Stefan adhesion forces and cavitation, and automating the generation of viaduct geometries and injection profiles to accelerate iCLIP printing. Future work in extending iCLIP to new materials and geometries will focus on testing a wider library of viscous filled resins with superior mechanical and electrical properties for applications in smart and sensor-embedded product designs, along with developing predictive models for analyzing the mechanical properties of multi-material iCLIP structures for applications in 4D printing and soft robotics, among other areas.

Materials and Methods:

Design of a prototype iCLIP printer

For print platform motion, a NEMA 57 stepper motor supplied by a 12V power bank was used to drive vertical build platform translation along a 12-inch Stroke Linear Motion Router (VXB Ballbearings, Anaheim, CA, USA). The UV light engine used was a 3DLP9000 (Digital Light Innovations, TX, USA) with a 4 million pixel 2560×1600 digital micromirror device (DMD), configured with a 385 nm LED and a $30 \mu\text{m}$ field of view (FOV) projection lens, with a total projection area of $76.8 \text{ mm} \times 48 \text{ mm}$. The light engine is a combination of a digital micromirror device (DMD) chip set (DLP9000, Texas Instrument, TX) along with a projection lens; the intrinsic specification of the DMD chipset is 385 nm ultraviolet (UV) wavelength, 2560×1600 DMD array, $7.6 \mu\text{m} \times 7.6 \mu\text{m}$ pixel size, build area of $19.5 \text{ mm} \times 12.2 \text{ mm}$; the projection lens diverges the UV projection to a 2560×1600 array of $30 \mu\text{m} \times 30 \mu\text{m}$ pixels to a build area of $76.8 \text{ mm} \times 48.0 \text{ mm}$ at a working distance of 126.5 mm. The printer was coordinated with an Arduino MEGA 2560 microcontroller and RAMPS 1.4 shield running open-source Marlin firmware. Custom software, written in C++ and implemented in the Qt Integrated Development Environment to provide a graphical user interface, allowed for tailoring UV light intensity, UV exposure time, stage speed and acceleration, layer thickness, and delay time after layers, within and between prints.

Resin formulations

For print speed and resin viscosity experiments, resins of tuneable viscosity were prepared by mixing isobornyl methacrylate, bisphenol A ethoxylated acrylate, and bisphenol A glycidyl methacrylate at varying ratios with 0.7 weight percent phenylbis(2,4,6-trimethylbenzoyl)phosphine oxide and 0.06 weight percent UV absorber 2-*tert*-butyl-6-(5-chloro-2H-benzotriazol-2-yl)-4-methylphenol (BLS 1326), all from Sigma Aldrich (St. Louis, MO, USA), using a Thinky planetary mixer (Thinky USA, Inc., Laguna Hills, CA, USA). Elastomeric resin formulation was prepared with varying ratios of epoxy aliphatic acrylate (EAA, tradename Ebecryl 113) and aliphatic urethane-based diacrylate (AUD, tradename Ebecryl 8413), which were purchased from Allnex (Malaysia), diluted in isobornyl acrylate and mixed with 1.0 weight percent photoinitiator diphenyl(2,4,6-trimethylbenzoyl)phosphine oxide (TPO).

Load cell measurements

The build platform was designed to accommodate a Miniature S-Beam Jr. Load Cell 2.0 (Futek, Irvine, CA, USA) of dimensions $0.75'' \times 0.69'' \times 0.26''$, with a resolution of ± 0.05 percent, a rated output of 1 mV/V (250 g) to 2 mV/V (1 – 100 lb), a bandwidth of 2,000 cycles per second, and with signal processing via a USB Load Cell Digital Amplifier (Futek, Irvine, CA, USA). Measurements were taken at 100 Hz. Force data was obtained midway through the print, i.e., once the build platform had fully exited the resin vat such that buoyancy forces did not change between layers.

Computational Fluid Dynamics Simulations

To control multi-material iCLIP printing, the flow within the deadzone was simulated using commercially available CFD software (ANSYS Fluent, Canonsburg, PA, USA). The resin was simulated as a homogenous fluid with a non-Newtonian viscosity profile. The fluid was given a density of 1120 kg/m^3 . The computational domain consisted of the vat resin and deadzone, modelled as fluid, and the printed object, as solid. The domain was discretized using an unstructured, hexahedral cell mesh comprised of a Cartesian core mesh. A no-slip boundary condition was prescribed on the deadzone-window interface. At the viaduct inlet of the computational domain, a mass influx profile is applied corresponding to the prescribed flow rate. The steady-state solution of the flow within the iCLIP printer is obtained by solving the conservation of mass and momentum equations on the computational mesh. Meshes were generated with an element size of 0.01 mm. Simulations were either run as static, when validating against injection calibration experiments, or dynamic, when guiding multi-material prints.

Mechanical Testing

Before testing, prints were post-processed by washing with 99% isopropanol, wicking away excess resin with Kimwipes, and post UV curing either by irradiating in an APM LED UV CUBE II oven (APM Technica, Switzerland, 365 nm), or with a handheld Loctite CureJet UV LED Controller (Henkel Corp., Dusseldorf, Germany).

Tensile testing of iCLIP-fabricated ASTM D638 type V dog bones, assessed for dimensional accuracy using a micrometer, was conducted using an Instron 5566 (Universal Testing Systems, Stoneham, MA, USA) with a cross-head speed of 1 mm/min at 25 °C to achieve the break at roughly 60 s, which is in accordance to the 30 s – 5 min outlined in ASTM D638, with a 100 N load cell. Tensile strength was calculated using the maximum load of the stress/strain curve and Young's modulus using the linear portion of the stress/strain curve.

Mechanical properties tests of composite prints were performed with an MTS Criterion Model 42 Universal Testing machine (MTS Systems Corporation, Eden Prairie, MN, USA), equipped with a 100 N load cell and either with fixtures for 3-point bending or platens for uniaxial and transverse compression. For uniaxial cyclic compression tests, the specific energy absorption of the cylindrical specimens (in J/kg) was calculated as the energy dissipated (from the area between the loading and unloading curves in the hysteresis loop) per unit mass.

Acknowledgements: Imaging experiments for this work were performed at the Molecular Imaging Program at Stanford (MIPS). Mechanical testing was performed at the Blume Center for Earthquake Engineering at Stanford. For printer design and prototyping, part of this work was performed at the Biodesign Collaboratory, supported by the Stanford Byers Center for Biodesign. For rheological characterization, part of this work was performed at the Stanford Soft Matter Facility (SMF).

Funding: This work is supported in part by the Precourt Institute for Energy at Stanford University. GL is supported by a graduate fellowship from the National Science Foundation.

Author contributions: GL built the printer, performed experiments, executed simulations, illustrated schematics, and wrote the manuscript. TS wrote printer software. ES, GL, and KH formulated lubrication theory. GL designed the printer. GL, IC, MTD, and WP developed resin formulations. WP and GL took photographs. All edited the manuscript. JMD conceptualized and directed the project.

Competing interests: JMD declares that he has an equity stake in Carbon Inc., which is a venture-backed startup company that owns related US Patent 9,216,546, US Patent 9,360,757 and others. LT reports a relationship with Digital Light Innovations that includes: employment, equity or stocks, and non-financial support. Methods for multi-material iCLIP are the subject of a pending patent application. The authors declare no other competing interests.

Data and materials availability: We report that at the time of submission to the Proceedings, in August of 2022, part of the work presented here is accepted for publication in the journal *Science Advances*.

References

-
- [1] J. Huang, Q. Qin, J. Wang. “A Review of Stereolithography: Processes and Systems” *Processes*. 8(9), 1138 (2020).
- [2] J. Tumbleston, D. Shirvanyants, N. Ermoshkin, R. Januszewicz, A. Johnson, D. Kelly, K. Chen, R. Pinschmidt, J. Rolland, A. Ermoshkin, E. Samulski, J. DeSimone, “Continuous liquid interface production of 3D objects” *Science* 347(6228),1349–1352 (2015).
- [3] R. Januszewicz, J. Tumbleston, A. Quintanilla, S. Mecham, J. DeSimone, “Layerless fabrication with continuous liquid interface production” *Proc Natl Acad Sci* 113, 11703–11708 (2016).
- [4] A. Johnson, C. Caudill, J. Tumbleston, C. Bloomquist, K. Moga, A. Ermoshkin, D. Shirvanyants, S. Mecham, C. Luft, J. DeSimone, “Single-Step Fabrication of Computationally Designed Microneedles by Continuous Liquid Interface Production” *PLoS ONE* 11(9): e0162518 (2016).
- [5] H. Ware, C. Sun, “Method for Attaining Dimensionally Accurate Conditions for High-Resolution Three-Dimensional Printing Ceramic Composite Structures Using MicroCLIP Process” *J. Micro Nano-Manufacturing* 7,031001 (2019).
- [6] A. Bhanvadia, R. Farley, Y. Noh, T. Nishida. “High-resolution stereolithography using a static liquid constrained interface” *Nature Communications Materials* 2(41) 3874 (2021).
- [7] D. Walker, J. Hedrick, C. Mirkin, “Rapid, large-volume, thermally controlled 3D printing using a mobile liquid interface” *Science* 80(366), 360–364 (2019).
- [8] J. Bachmann, E. Gleis, G. Fruhmann, J. Riedelbauch, S. Schmolzer, O. Hinrichsen. “Photo-differential scanning calorimetry parameter study of photopolymers used in digital light synthesis” *Addit. Manuf.* 37, 101677 (2021).
- [9] C. Caudill, J. Perry, S. Tian, J. Luft, J. DeSimone, “Spatially controlled coating of continuous liquid interface production microneedles for transdermal protein delivery” *J. Control. Release* 284, 122–132 (2018).
- [10] C. Caudill, J. Perry, I. Kimon, A. Tessema, B. Lee, B. Mecham, S. Tian, J. DeSimone, “Transdermal vaccination via 3D-printed microneedles induces potent humoral and cellular immunity” *Proc. Natl. Acad. Sci. U. S. A.* 118, (2021).
- [11] Y. Huang, C. Jiang, “On-line force monitoring of platform ascending rapid prototyping system” *J. Mater. Process. Technol.* 159, 257–264 (2005).
- [12] Q. Wang, Y. Sun, B. Guo, P. Li, Y. Li, “CFD analysis and prediction of suction force during the pulling-up stage of the continuous liquid interface production process” *AIP Adv.* 9, 015225 (2019).
- [13] Y. Pan, H. He, J. Xu, A. Feinerman, “Study of separation force in constrained surface projection stereolithography” *Rapid Prototyp. J.* **23**, 353–361 (2017).

-
- [14] L. Wang, Y. Luo, Z. Yang, W. Dai, X. Liu, J. Yang, B. Lu, L. Chen, “Accelerated refilling speed in rapid stereolithography based on nano- textured functional release film” *Addit. Manuf.* **29**, 100791 (2019).
- [15] X. Li, H. Mao, Y. Pan, Y. Chen, “Mask Video Projection-Based Stereolithography with Continuous Resin Flow” *J. Manuf. Sci. Eng. Trans. ASME* **141**, (2019).
- [16] J. Hardin, T. Ober, A. Valentine, J. Lewis, “Microfluidic printheads for multimaterial 3D printing of viscoelastic inks.” *Adv. Mater.* **27** (2015).
- [17] M. Skylar-Scott, J. Mueller, C. Visser, J. Lewis, “Voxelated soft matter via multimaterial multinozzle 3D printing” *Nature* **575** (2019).
- [18] A. Rutz, K. Hyland, A. Jakus, W. Burghardt, R. Shah, “A multimaterial bioink method for 3D printing tunable, cell-compatible hydrogels” *Adv. Mater.* **27** 1607–1614 (2015).
- [19] D. Dendukuri, P. Panda, R. Haghgooie, J. Kim, T. Hatton, P. Doyle, “Modeling of Oxygen-Inhibited Free Radical Photopolymerization in a PDMS Microfluidic Device” *Macromolecules* **41**, 8547–8556 (2008).